Electrochimica Acta 415 (2022) 140260

Contents lists available at ScienceDirect

Electrochimica Acta

journal homepage: www.journals.elsevier.com/electrochimica-acta

Development of an Al^{3+} ion-selective microelectrode for the potentiometric microelectrochemical monitoring of corrosion sites on 2098−T351 aluminum alloy surfaces

Rejane Maria P. da Silva [a,*], Javier Izquierdo [b,c], Mariana X. Milagre [a], Renato A. Antunes [d], Ricardo M. Souto [b,c,**], Isolda Costa [a,*]

[a] Instituto de Pesquisas Energéticas e Nucleares, IPEN/CNEN, Av. Prof. Lineu Prestes, 2242 São Paulo, Brazil
[b] Department of Chemistry, Universidad de La Laguna, P.O. Box 456, La Laguna (Tenerife), E-38200 Canary Islands, Spain
[c] Institute of Material Science and Nanotechnology, Universidad de La Laguna, P.O. Box 456, La Laguna (Tenerife), E-38200 Canary Islands, Spain
[d] Centro de Engenharia, Modelagem e Ciências Sociais Aplicadas (CECS), Universidade Federal do ABC (UFABC), Av. dos Estados 5001, 09210-580 Santo André, SP, Brazil

ARTICLE INFO

Keywords:
Ion-selective microelectrode
SECM
Corrosion
Aluminum
Al−Cu−Li alloys
Friction stir welding

ABSTRACT

A novel potentiometric Al^{3+}−ion selective microelectrode (ISME), with internal solid contact, based on the use of a neutral carrier morin as ionophore is reported. The ability of the ISME to image local ion concentration distributions was tested on aluminum alloy surfaces freely corroding in an aqueous solution containing chloride ions. The microelectrode was then used as the sensing tip for scanning electrochemical microscopy (SECM) in potentiometric operation to monitor the reactive sites associated with the dissolution of aluminum that developed in the 2098−T351 Al−Cu−Li alloy as a result of welding by the Friction Stir Welding (FSW) process. The ISME detected differences in the local concentrations of Al^{3+} species arising from the 2098−T351 Al−Cu−Li alloy (base material) and from the coupled weld joint/heat affected zones (WJ/HAZ) of the alloy produced by the FSW process. More active domains for Al^{3+} dissolution were found in the HAZ regions coupled to WJ, more specially in the HAZ of the advancing side (AS). These results demonstrate that the Al^{3+}−ISME presented in this work can be used to monitor corrosion sites on aluminum alloys surfaces with combined chemical and spatial resolution.

1. Introduction

Designing materials tailored to specific mechanical requirements that contain complex microstructures requires surface analysis techniques with higher resolution and specificity for their characterization. This is the case of the aluminum alloys used in the automotive and aerospace industries [1], and especially for the third generation of Al−Cu−Li alloys [2] of low density, good mechanical resistance and tenacity [3,4]. These alloys are becoming a commercial success to replace conventional 2XXX series alloys (such as 2024 and 2219) in pressurized cabins, fuselage and internal structure of the aircraft, in order to reduce the aircraft weight and consequently, fuel consumption [3–5]. Unfortunately, Al−Cu−Li alloys are very sensitive to localized corrosion due to the high electrochemical activity of the T1 phase (Al_2CuLi) present in their complex microstructures [5–7]. The rapid selective dissolution in aggressive environments of this phase leads first to the enrichment of copper, followed by the reversal of polarity and finally to dissolution of the aluminum matrix [5,6,8]. In addition, changes occur in the microstructure of the alloy during welding, resulting in local modification of its physicochemical characteristics [9, 10], including the appearance of microgalvanic coupling processes and corrosion susceptibility between the distinct zones formed during

Abbreviations: SECM, Scanning electrochemical microscopy; ISME, Ion selective microelectrode; FSW, friction stir welding; WJ/HAZ, weld joint/heat affected zones; AS, advancing side; RS, retreating side; XPS, X-ray Photoelectron Spectroscopy; TMAZ, thermomechanically affected zone; SZ, stir zone; HAZ, heat affected zone; SLC, severe localized corrosion.

* Corresponding authors.
** Corresponding author at: Department of Chemistry, Universidad de La Laguna, P.O. Box 456, E-38200 La Laguna (Tenerife), Canary Islands, Spain
E-mail addresses: rejanep2silva@gmail.com (R.M.P. da Silva), rsouto@ull.es (R.M. Souto), icosta@ipen.br (I. Costa).

https://doi.org/10.1016/j.electacta.2022.140260
Received 30 October 2021; Received in revised form 14 February 2022; Accepted 19 March 2022
Available online 21 March 2022

welding [7,11]. Among welding procedures, friction stir welding (FSW) is a solid state process that has shown great potential as a welding procedure for difficult-to-weld materials using conventional processes such as aluminum alloys [9]. However, the FSW process changes the microstructure of the base material by thermal and mechanical effects, causing various zones with different microstructures to form [9,10].

The spatially resolved study of localized corrosion processes is achieved by scanning electrochemical microscopy (SECM) [12–14]. For this purpose, SECM is generally used in the amperometric mode using Pt probes, although the applicability of these probes is limited by the onset of hydrogen evolution and oxygen reduction reactions. This is a major limitation for the characterization of materials with very negative redox potentials, such as aluminum, magnesium and zinc in aqueous environments [15–18]. Since local concentration variations in molecular and ionic species occur in the adjacent liquid phase as a result of corrosion, these systems can be investigated by SECM in potentiometric mode using an ion-selective microelectrode (ISME) as the probe [19]. In this way, distribution images of particular ionic species generated at the anodic sites of a corroding surface with high chemical selectivity were obtained for a variety of metal systems [20–25]. The use of an internal solid contact has resulted in more robust, lower internal resistance and faster response times [22,24], while test procedures were designed to minimize potential interference from local electric fields [26,27] or from other chemical species [28], leading to improved ISME chemical resolution. However, no reports can be found in the literature on the use of ion-selective microelectrodes to monitor local distributions of Al^{3+} concentration generated by corrosion processes, and studies on the corrosion of aluminum-based materials were carried out mainly in amperometric mode [5,29–33] to monitor hydrogen evolution and oxygen reduction reactions on the reactive surfaces, while the potentiometric mode was adopted exclusively for the detection of local pH changes [34]. But there are reports of ion-selective electrodes (ISE's) based on a poly(vinyl chloride) membrane for various inorganic ions [35–37], including direct monitoring of aluminum in the medical, environmental and industrial sectors [38–44]. Among them, Gupta et al. [41] developed an Al^{3+} selective potentiometric sensor (macroelectrode) based on morin in a poly(vinyl chloride) matrix for analytical applications. Morin is known to form a strong complex with aluminum that can be employed as a selective aluminum ionophore [41].

In this work we report the first results of the development and application of an Al^{3+}−ISME, with internal solid contact, for the potentiometric monitoring by SECM of the reactive sites associated with the dissolution of aluminum in the 2098−T351 Al−Cu−Li alloy welded using the FSW technique. To the authors' knowledge, the use an ISME for the SECM study of Al^{3+} concentration distributions resulting from corrosion processes occurring on aluminum alloy surfaces in aqueous media has not been reported in the literature. This new ISME was developed employing neutral carrier morin as ionophore, while solid contact was obtained by replacing the internal reference electrode with a carbon fiber immersed in the ionophore cocktail [22–24]. In this way, it was possible to monitor Al^{3+}concentration distributions resulting from the corrosion processes that occur on 2098-T351 aluminum alloy in aqueous environment. The electrochemical results were correlated with the high-resolution Al2p spectra measured by X-ray Photoelectron Spectroscopy (XPS) on the studied surfaces.

2. Experimental

2.1. Material and reagents

The 2098−T351 Al−Cu−Li alloy welded by FSW process [45] and its base material (wt%: 3.4 Cu, 1.0 Li, 0.3 Mg, 0.3 Ag, 0.4 Zr, 0.04 Fe, 0.05 Si, 0.02Zn, 0.003 Mn) were investigated in the polished condition. To do this, the alloy surfaces were successively ground with 320, 550, 800, 1200 and 4000 grit SiC paper, followed by polishing with diamond slurries of 3 and 1 μm size.

All experiments were performed using ultra-pure analytical grade reagents: Sodium chloride(Panreac®), morin(Sigma-Aldrich®), poly (vinyl chloride(Supelco®), sodium tetraphenyl borate(Supelco®), tri−*n*−butylphosphate(SAFC®) and tetrahydrofurane(Sigma-Aldrich®).

2.2. Microstructural and surface characterization

Surface observations were performed on 2098-T351 aluminum alloy after the corrosion tests using a Leica optical microscope. High-resolution Al2p spectra were obtained by X-ray photoelectron spectroscopy (XPS). XPS spectra were obtained using a Thermo Fisher Scientific K-Alpha+ spectrometer operating with a monochromatic Al K-α X-ray source (Waltham, MA, USA). The pressure in the analysis chamber was approximately 10^{-7} Pa. The binding energy scale was calibrated with base on the adventitious C1s peak at 284.8 eV. High resolution Al2p spectra of the 2098-T351 alloy surfaces were obtained before and after immersion in 5 mmol L^{-1} NaCl solution for 72 h.

2.3. Preparation of the Al^{3+}- ion-selective microelectrode (Al^{3+}−ISME)

The components of the ionophore cocktail used in the fabrication of the Al^{3+}−ISME were morin, poly-vinyl-chloride (PVC), sodium tetraphenyl borate and tri-*n*-butylphosphate in the composition ratio 5:20:5:150 (w/w, mg). 1.0 mL tetrahydrofuran (THF) was used for the dissolution of the components.

In the first step, micropipettes were pulled from borosilicate capillaries (outer $\varnothing$ = 1.5 mm, wall thickness $\varnothing$ = 0.225 mm; Hilgenberg GmbH, Malsfeld, Germany) using a P-30 micropipette puller (Sutter Instrument, Novato, CA, USA). The opening diameters at the tip of the micropipettes typically ranged between 20 and 35 μm. After soaking in "piranha solution", the capillaries were silanized using 5% dimethyldichlorosilane in heptane, followed by thorough washing with deionized water and ethanol, and subsequent drying in the oven at 80 °C for 120 min. The solid contact with the ionophore coating was achieved using a 30 μm diameter carbon fiber coated with a conducting polymer. The application of the coating on the carbon fibers was performed through an electrochemical route using 3,4−ethylenedioxythiophene (EDOT, HC Starck GmbH, Goslar, Germany) dissolved in 1−butyl−3−methylimidazolium hexafluorophosphate ($BMIM^+$ PF_6^-) ionic liquid [19]. For that purpose, the carbon fiber of approximately 3.0 cm length, attached to a copper wire with silver epoxy adhesive, is connected as the working electrode with an Ag/AgCl wire as reference electrode, and a platinum wire as auxiliary electrode. Finally, the hydrofobized capillaries were backfilled with the aluminum selective cocktail with suction, and the PEDOT-coated carbon fiber was inserted into the cocktail as close to the orifice of the tip as possible, while the upper part of the micropipette was closed with Loctite adhesive. More details on the fabrication of solid contact ISME's are described elsewhere [23,24]. The Al^{3+}−ISME was calibrated using $Al(NO_3)_3$ solutions in the concentration range of 10^{-6} to 10^{-1} mol L^{-1}, to determine an interval showing a linear relationship between $pAl = -\log_{10}[Al^{3+}]$ and the potential response. Good reproducibility was observed by building various Al^{3+}−ISME's and comparing their calibration plots in this studied concentration range. A response time of 240 ms was determined using the procedure described elsewhere [24]. Special attention was paid to study an eventual chemical interference of the solution pH on the potential response of the Al^{3+}−ISME, but no significant effect was found in the range $3 < pH \leq 11$ that takes place in the system under study [7].

2.4. Scanning electrochemical microscopy (SECM) in potentiometric operation mode

The potentiometric operation mode was performed using a high-resolution SECM device (Sensolytics, Bochum, Germany), connected to an Autolab electrochemical interface (Metrohm, Herisau, Switzerland), and controlled by a conventional computer. In the measurement circuit,

a voltage follower based on a 10^{13} input impedance operational amplifier (TL071, Texas Instruments, Dallas, TX, USA) was inserted. The potentiometric measurements were carried out at room temperature applying this configuration. During the measurements, the 2098-T351 aluminum alloy surfaces remained effectively unpolarized (in their spontaneous open circuit). The Al^{3+}−ISME was used as the scanning tip to monitor Al^{3+} distributions developing on corroding surfaces. In all potentiometric measurements, the electrochemical cell consisted of the Al^{3+}−ISME and an Ag/AgCl/KCl (sat.) reference electrode. For the potentiometric SECM measurements, the Al^{3+}−ISME was positioned at a height of approximately 50 μm above the investigated surfaces. This vertical tip-substrate distance was established using the gentle approach procedure using a TV camcorder system. Next, SECM potentiometric scans were recorded while the ISME tip was moved in an *XY* plane parallel to the surface of the 2098-T351 aluminum alloy under study. Therefore, the consecutive scan lines that make up the *XY* grid were recorded at the constant tip-substrate distance of 50 μm.

3. Results and discussion

Fig. 1a shows an optical micrograph of the Al^{3+}−ISME developed in this work, whereas its calibration curve is shown in Fig. 1b as a function of pAl. A good linear relationship between the potential response of the ISME and pAl was observed in the range $1 \leq pAl \leq 5$. However, no considerable variation in potential responses was observed for $Al(NO_3)_3$ solutions at concentrations lower than 10^{-6} mol L^{-1}. As seen in Fig. 1b, the point corresponding to this lower concentration is outside the linearity range. For the linear range ($1 \leq pAl \leq 5$), the slope obtained was of −18.8 mV $decade^{-1}$, a value close enough to the expected Nernstian value of 19.7 mV $decade^{-1}$ to use this ISME for quantitative analysis. The calibration equation describing the linear part of the calibration plot is given by the following equation (in mV):

$$E_{ISME} = 246.6 - 18.8\,pAl \quad (1)$$

After verifying the performance of the Al^{3+}−ISME, the microelectrode was employed to monitor the local concentration distributions of Al^{3+} ions associated with local corrosion on the 2098-T351 alloy (base material) exposed to 5 mmol L^{-1} NaCl solution. This test solution was selected as a compromise between the time needed to collect a 2D array scan map over a significant area extending over two coupled areas along the weld and a solution composition aggressive enough for the corrosion process to start, but not at such a high corrosion rate that significant changes to the surface would be occurring during the time needed to complete one map. The SECM map shown in Fig. 2 was recorded after approximately 60 min of exposure to the 5 mmol L^{-1} NaCl solution. They show a localized corrosive attack on the alloy surface. The lower and upper color scales for the 2D maps are an indication of the Al^{3+}activity in the liquid phase in the proximity of the 2098−T351 surface. The red color of the scale is associated with the regions with more active domains for Al^{3+}, in which there has been a greater dissolution of aluminum. The oxidation of Al^0 to Al^{3+} in aerated and neutral aqueous environments occurs in the anodic regions according to:

$$Al \rightarrow Al^{3+} + 3e^- \quad (2)$$

whereas the main cathodic reaction is the oxygen reduction reaction:

$$O_2 + 2H_2O + 4e^- \rightarrow 4OH^- \quad (3)$$

When aluminum alloys are exposed to aerated solutions containing Cl^- ions, localized corrosion is favored. The galvanic coupling of the matrix with cathodic/anodic intermetallic particles favors the dissolution process in these aluminum alloys [6−8]. Further progress of the corrosion reaction at the severe localized corrosion (SLC) site leads to the measurement of even higher aluminum ion activities in the electrolyte adjacent to the alloy that are observed in the more focused 2D map given at the right in Fig. 2. In both situations presented in Fig. 2, the high electrochemical activity of same SLC site developed on the alloy surface was observed. It has been demonstrated that the onset of a SLC site on the surface of the material continues propagating with the elapse of the time without any sign of repassivation in this electrolyte solution.

Fig. 3 shows an optical image of the 2098−T351 surface retrieved after the acquisition of the SECM images shown in Fig. 2. Localized corrosion features on the surface associated with severe localized corrosion (SLC) are observed [5−7]. As it was mentioned above, Al−Cu−Li alloys are very sensitive to the development of SLC sites, which are directly associated with the hexagonal T1 phase (Al_2CuLi) [5,6,32]. In this process, propagation takes place along grain and sub-grain boundaries, and the dissolution of the aluminum and lithium present in the T1 phase, leads to the formation of copper-rich particles that act as cathodes, thus promoting the anodic dissolution of the matrix in the vicinity [6−8]. The SECM images presented in Fig. 2 show that the dissolution of aluminum was predominant in the region of localized corrosion. Thus, when the Al^{3+}−ISME passed over this region, it detected the Al^{3+} ions released at the anodic regions, as given by reaction (2).

The Al^{3+}−ISME was also used to image the local Al^{3+} concentrations

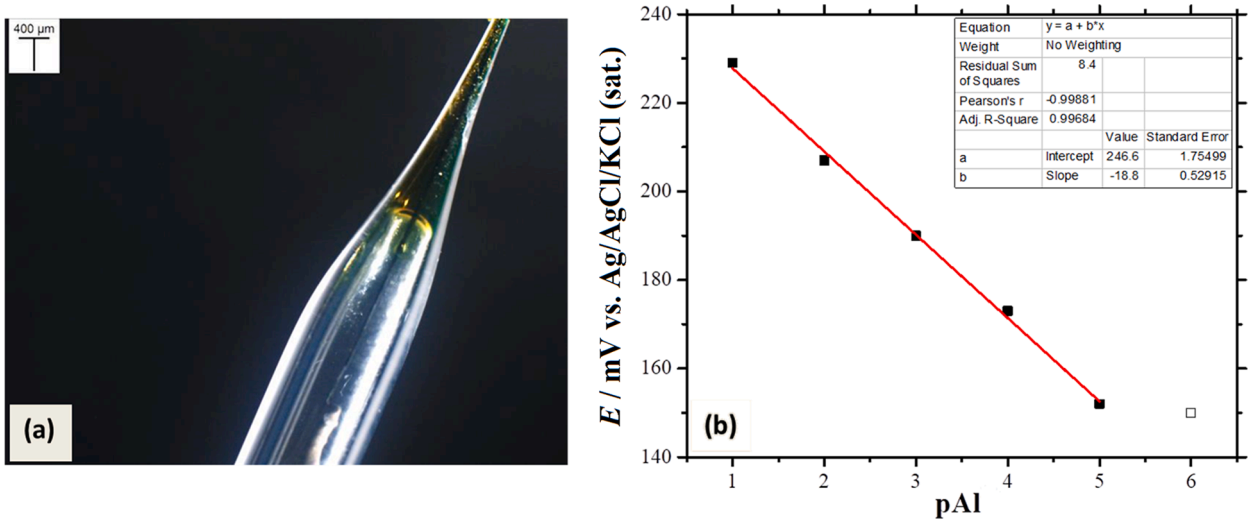

Fig. 1. Micrograph (a) and calibration plot (b) for the Al^{3+}−ion selective microelectrode (ISME) designed in this work. $pAl = -\log_{10}[Al^{3+}]$. The calibration plot was determined by measuring the potentiometric response of the ISME in a sequence of solutions containing increasing amounts of $Al(NO_3)_3$.

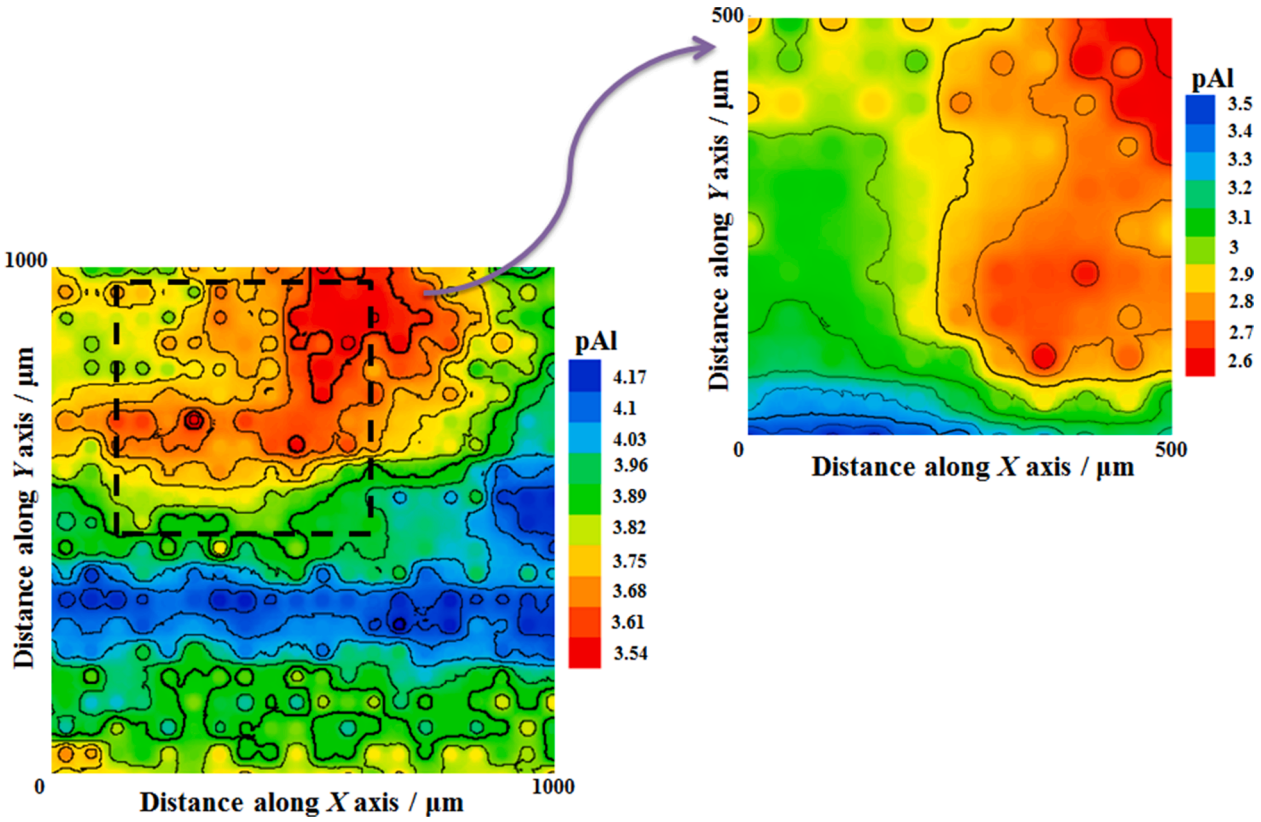

Fig. 2. SECM maps recorded over a freely corroding 2098-T351 for various immersion times in 5 mmol L^{-1} NaCl solution. The map at the left was recorded after approximately 60 min of exposure to the solution, whereas the second map was recorded immediately after although over a smaller portion of the surface that is approximately described by the black square. The images were obtained using an Al^{3+}−ISME for potentiometric SECM operation. Tip-substrate distance: 50 µm; scan rate: 50 µm s^{-1}; pAl = $-\log_{10}$ [Al^{3+}].

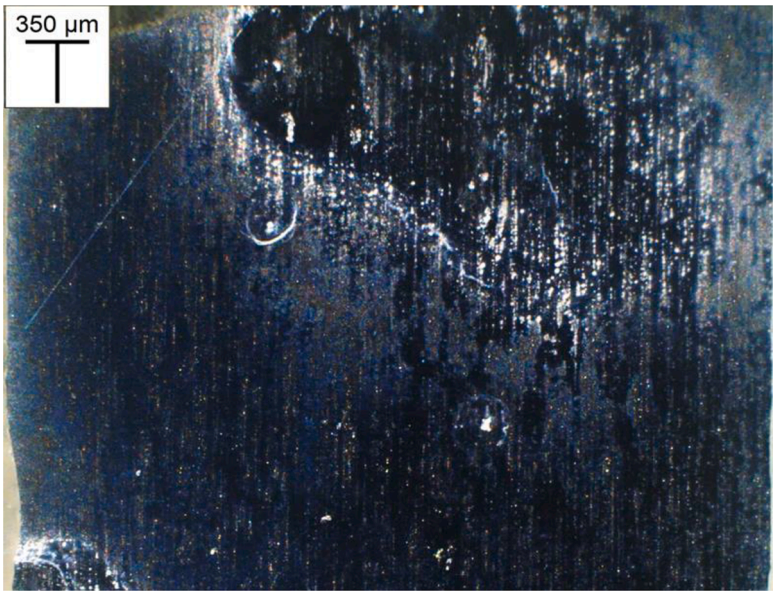

Fig. 3. Optical image of the 2098−T351 Al−Cu−Li alloy following retrieval from the solution after completion of the SECM analysis given in Fig. 2.

arising from the regions with different microstructural properties developed in the weld zone created in the alloy due to the FSW process, which have been already characterized using microhardness measurements [45]. In brief, a heat affected zone (HAZ), a thermomechanically affected zone (TMAZ), and a stir zone (SZ) were identified. In addition, some differences were also observed in the first two zones (i.e., HAZ and TMAZ) depending on whether they were located on the advancing side (AS) or the retreating side (RS) in the relative movement of the welding tool. Accordingly, the coupled welded zones WJ/HAZ(RS) and WJ/HAZ (AS) of the FSW 2098−T351 aluminum alloy were selected in this investigation.

The spatially-resolved pAl distributions at interfaces of the coupled

welded zones of the FSW 2098−T351 alloy were monitored during immersion in 5 mmol L^{-1} NaCl solution. 2D array scan maps recorded above the different welded zones of the FSW-2098−T351 alloy after approximately 120 min of exposure to the test solution obtained in this investigation are shown in Fig. 4, and show a corrosive attack with larger active domains for Al^{3+}dissolution in the HAZ regions coupled to the WJ zone. In the latter, the corrosion activity was lower compared to the HAZ regions and, therefore, the active domains for Al^{3+}were lower. Thus, in both sides of the weld (i.e., AS and RS), the HAZ was more susceptible to aluminum dissolution. As reported in our previous work [45], this region, when coupled to the WJ zone, is more sensitive to corrosion, mainly due to the effects of galvanic coupling. Thus, the HAZ was more sensitive to the formation of anodic sites than WJ, which exhibited higher cathodic activity. The optical micrographs recorded in these regions after SECM analysis, shown in Fig. 5, corroborate these observations, showing that corrosion activity was more intense in HAZ than in WJ (regardless of being RS or AS).

In Fig. 4, it is also observed that the activity for $Al^{3+}$was more intense on the AS side. As previously reported [45], a higher corrosion activity was found in the HAZ(AS) region compared to HAZ(RS), when these two regions were coupled to WJ. The SECM and SVET results revealed that the HAZ regions exhibited anodic behavior in relation to WJ. Furthermore, SVET analysis showed that the values of the ionic currents measured above HAZ(AS) region were about four times higher than those observed over HAZ(RS) under the same conditions [45]. Therefore, it is that greater dissolution of aluminum was expected to occur in this zone.

Next, sites with lower aluminum ion activity were observed in Fig. 4 over the WJ region compared to the larger sites found in the HAZ regions. This is because the cathodic Fe–Cu-rich particles favor trenching. The welding process promotes particle breakdown and the stirring of the weld tool drags the broken particles, effectively increasing the number of cathodic sites. Thus, within this zone, microgalvanic coupling between the adjacent matrix and the Fe−Cu enriched particles is favored [45]. In this way, the Al^{3+}−ISME was still able to detect the rather weak active domains for Al^{3+}dissolution occurring in this region.

For the immersed material, reactions are determined by the properties of the hydroxide/oxide layer formed on the surface. The composition of this layer is a mixture of oxides and hydroxides such as $Al(OH)_3$, AlOOH and Al_2O_3. Thus, this layer is considered to be in a state of equilibrium between dissolution and formation, and is characterized by its limited protective properties, as it is amorphous and porous [7,46]. These characteristics contribute to the low resistance to localized corrosion of the aluminum alloys in a corrosive environment [7,46]. In

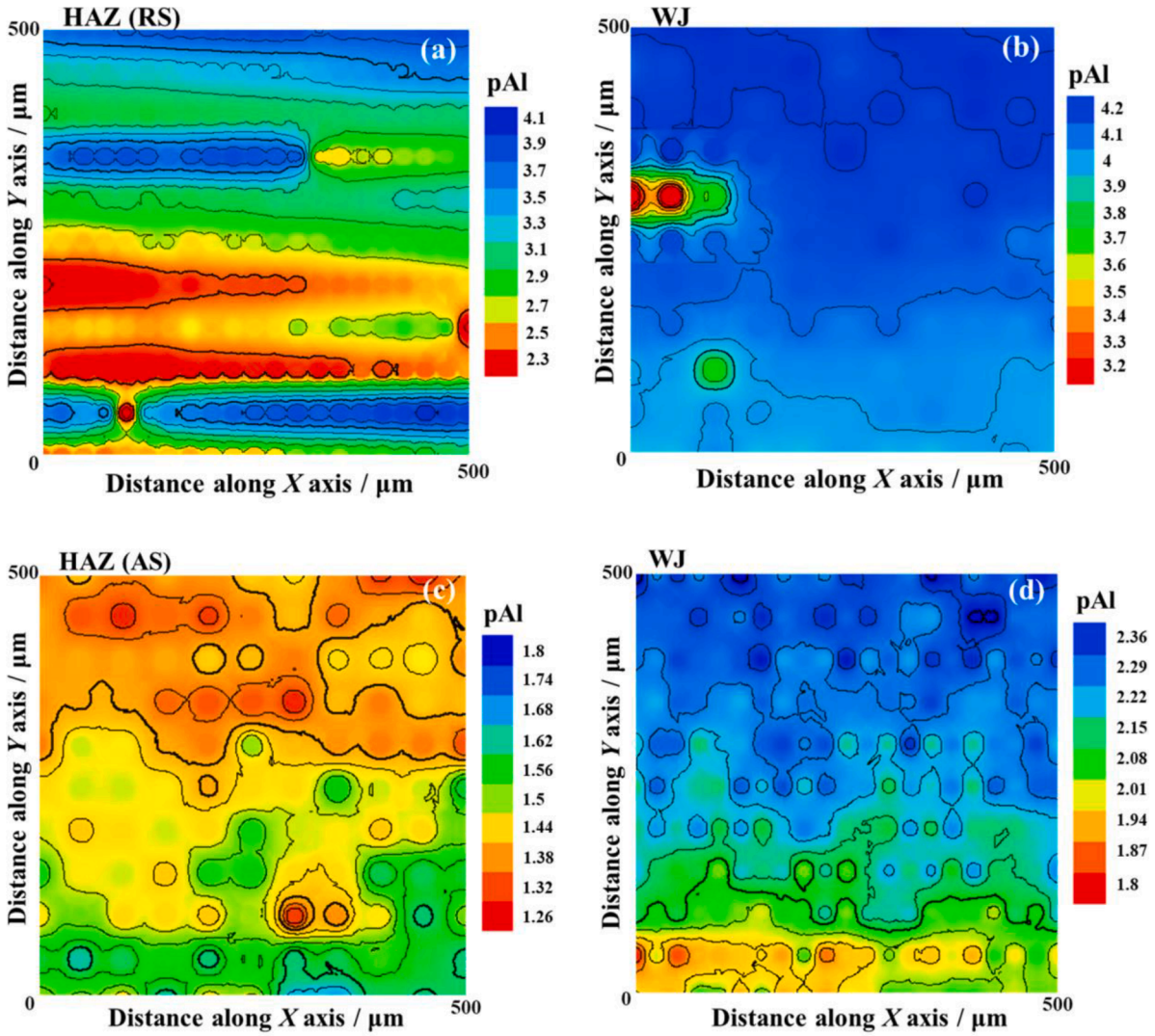

Fig. 4. SECM maps obtained above different welded zones identified on the FSW-2098-T351 alloy while freely corroding in aerated 5 mmol L^{-1} NaCl solution for approximately 120 min. The images were obtained using an Al^{3+}−ISME for potentiometric SECM investigation on the coupled weld joint/heat affected zones (WJ/HAZ) of the (a,b) retreating side (RS) and (c,d) advancing side (AS). Tip-substrate distance: 50 µm; scan rate: 50 µm s^{-1}; pAl = $-\log_{10}$ [Al^{3+}].

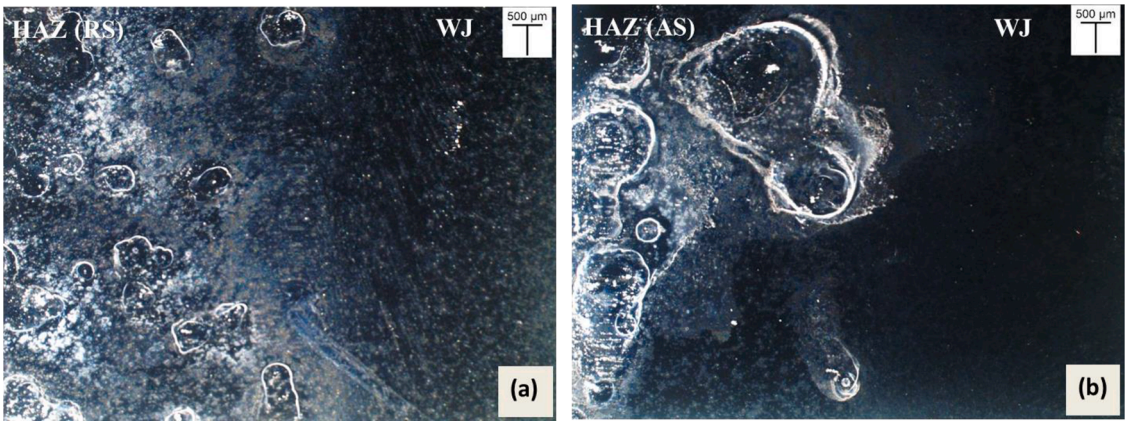

Fig. 5. Optical images of the coupled weld joint/heat affected zones (WJ/HAZ) of the (a) retreating side (RS)and (b) advancing side (AS) identified on the FSW 2098−T351 Al−Cu−Li alloy that were investigated during the potentiometric SECM tests of Fig. 4.

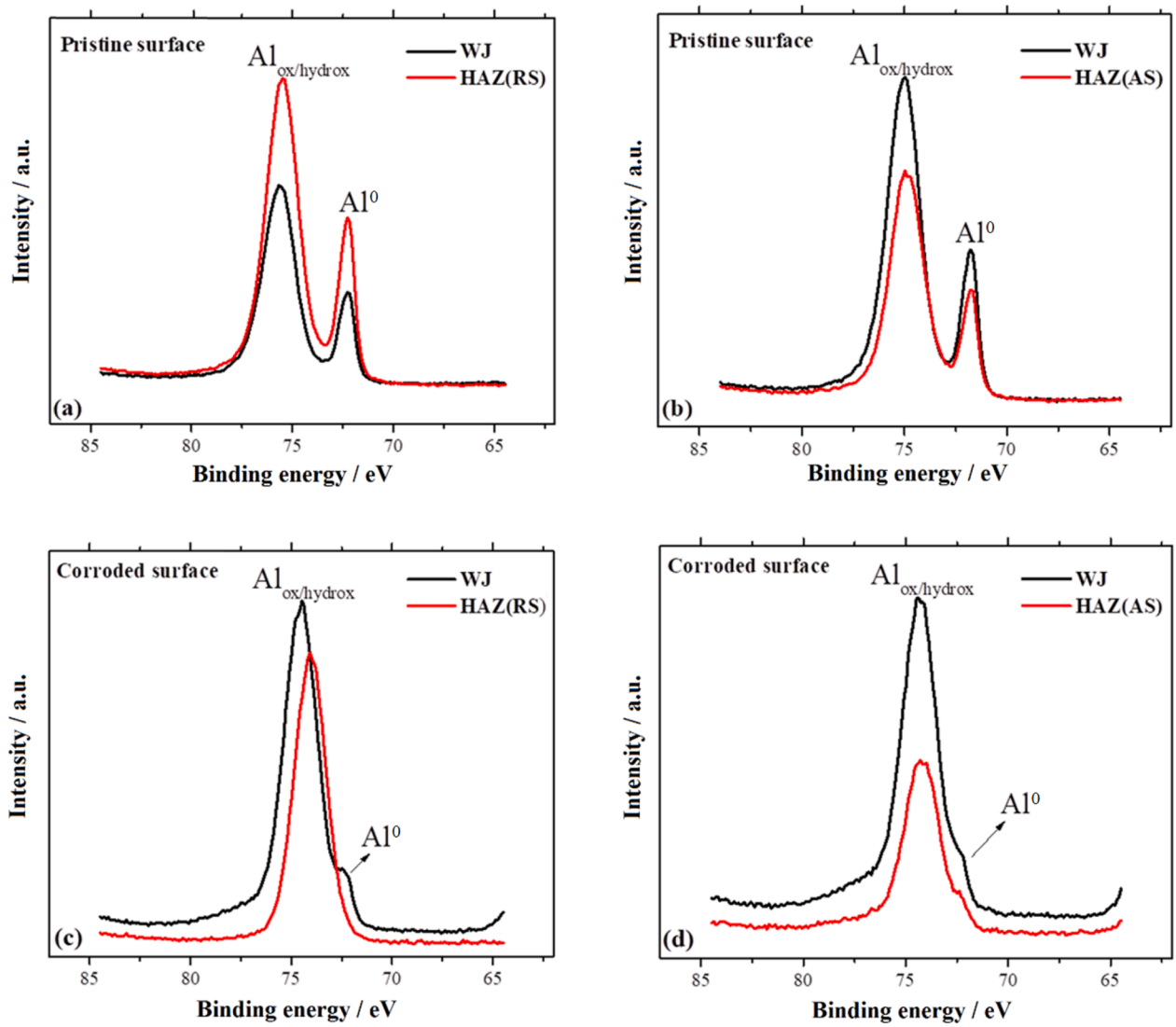

Fig. 6. High-resolution Al2p spectra acquired in the welding regions of the FSW 2098−T351 Al−Cu−Li alloy before (a,b) and after (c,d) the corrosion tests. Welding zones: (a,c) the joint/heat affected zones (WJ/HAZ) of the retreating side (RS), and (b,d) the joint/heat affected zones (WJ/HAZ) of the advancing side (AS).

Fig. 6a-b, the high resolution spectra obtained by XPS for the pristine alloy surface in the coupled welded zones described above, show Al2p peaks at approximately 74.0 eV corresponding to aluminum oxide/hydroxide [47]. After corrosion tests, the high resolution spectra in Fig. 6c-d also show Al2p peaks around 74.3 eV that can be attributed to the aluminum oxide/hydroxide layer [47]. But the Al2p signal

observed in the HAZ region was found to be weaker compared to that of the WJ, whether it corresponds to the RS or the AS. The highest Al2p signal observed in WJ is related to the oxide layer formed during the corrosion process, which tends to be more uniform in this region compared to HAZ. In WJ, the formation of OH^- is higher due to the cathodic behavior of this region. As result, the Al^{3+} ions generated at the trenching sites within this region easily combine with the available OH^- ions, forming the aluminum-enriched hydroxide/oxide. On the other hand, the HAZ that is anodic in relation to WJ [45], exhibited a greater susceptibility to undergo severe localized corrosion, in which the generation of Al^{3+} species is greater, but the volume of OH^- formed is less than in WJ, which acts as a macro-cathode. Therefore, the corrosion activity and, consequently, the dissolution of aluminum is lower in the WJ region, as seen in Fig. 5. This explains the low activity domains for Al^{3+}recorded in this region by the scanning Al^{3+}−ISME (cf. Fig. 4).

The XPS data also showed differences in terms of Al2p signal observed on the advancing side (AS) versus the retreating side (RS) of the HAZ (see Fig. 7). A higher Al2p peak in the HAZ(RS) shows that, in fact, the effect of the galvanic coupling was greater for the AS side. This is consistent with the potentiometric SECM maps shown in Fig. 4, in which the activity for the Al^{3+} local concentration distribution was more intense in the HAZ(AS) compared to HAZ(RS). Therefore, XPS data support the microelectrochemical results obtained with the Al^{3+}−ISME for SECM imaging in the potentiometric mode along the welding zones developed on 2098-T351 Al−Cu−Li alloy welded using the FSW process.

4. Conclusions

A novel ISME, with solid-contact, was presented for potentiometric microelectrochemical monitoring of corrosion sites on aluminum alloy surfaces. It is based on the use of neutral carrier morin as an ionophore. This microelectrode has been successfully applied to perform in situ experiments on corroding aluminum alloy surfaces during exposure to an aqueous saline solution.

This ISME was able to respond to the local concentrations of Al^{3+} arising from 2098−T351 Al−Cu−Li alloy welded by FSW process and its base material. More active domains for Al^{3+} were detected in the anodic regions associated with the dissolution of aluminum, mainly from the localized corrosion sites developed on the alloy. The HAZ regions coupled to WJ zone presented greater corrosion activity on the basis of the Al^{3+} local concentration distributions, that were associated to the effects of galvanic coupling between zones of different microstructure along the weld. However, on the advancing side (AS), the active domains for Al^{3+} were more intense compared to the retreating side (RS), due to increased electrochemical activity on the AS side.

Since no attempt has been made so far to use an Al^{3+}−ISME to study aluminum dissolution from Al−Cu−Li alloys undergoing corrosion, the proposed ISME is considered an important addition in the field and can be used for the spatially-resolved microelectrochemical monitoring of local concentrations of Al^{3+} around corroding surfaces in aqueous environments.

CRediT authorship contribution statement

Rejane Maria P. da Silva: Conceptualization, Investigation, Data curation, Validation, Visualization, Writing – original draft, Writing – review & editing. **Javier Izquierdo:** Data curation, Supervision, Visualization, Methodology, Writing – review & editing. **Mariana X. Milagre:** Investigation, Writing – review & editing. **Renato A. Antunes:** Investigation, Writing – review & editing. **Ricardo M. Souto:** Data curation, Supervision, Methodology, Funding acquisition, Writing – original draft, Writing – review & editing. **Isolda Costa:** Supervision, Resources, Funding acquisition, Writing – review & editing.

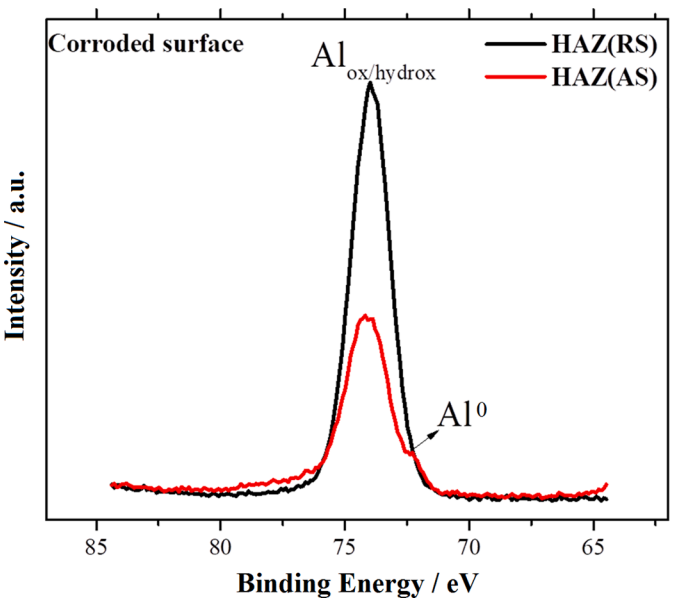

Fig. 7. High-resolution Al2p spectra obtained in the heat affected zones (HAZ), for both the advancing (AS) and the retreating (RS) sides of the FSW 2098−T351 Al−Cu−Li alloy after the corrosion tests.

Declaration of Competing Interest

The authors declare that they have no known competing financial interests or personal relationships that could have appeared to influence the work reported in this paper.

Acknowledgments

The authors acknowledge Fundação de Amparo à Pesquisa do Estado de São Paulo- FAPESP (Proc. 2013/13235−6, Proc.2018/06880−6 and Proc. 2019/11427−1) for financial support, the Spanish Ministry of Economy and Competitiveness (MINECO, Madrid, Spain) and the European Regional Development Fund (Brussels, Belgium) under grant CTQ2016−80522−P. The Multiuser Central Facilities (CEM) of UFABC is acknowledged for the experimental support.

References

[1] F.M. Mazzolani, Aluminium Alloy Structures, 2nd edition, Chapman & Hall, London, 1995, p. 693.
[2] T. Warner, Recently-developed aluminium solutions for aerospace applications, Mater. Sci. Forum 519–521 (2006) 1271–1278, https://doi.org/10.4028/www.scientific.net/MSF.519-521.1271.
[3] H.G. Salem, J.S. Lyons, Effect of equal channel angular extrusion on the microstructure and superplasticity of an Al-Li alloy, J. Mater. Eng. Perform. 11 (2002) 384–391, https://doi.org/10.1361/105994902770343908.
[4] P.S. De, R.S. Mishra, J.A. Baumann, Characterization of high cycle fatigue behavior of a new generation aluminum lithium alloy, Acta Mater. 59 (2011) 5946–5960, https://doi.org/10.1016/j.actamat.2011.06.003.
[5] M.X. Milagre, U. Donatus, C.S.C. Machado, J.V.S. Araujo, R.M.P. Silva, B.V.G. de Viveiros, A. Astarita, I. Costa, Comparison of the corrosion resistance of an Al–Cu alloy and an Al–Cu–Li alloy, Corros. Eng., Sci. Technol. 54 (2019) 402–412, https://doi.org/10.1080/1478422X.2019.1605472.
[6] R.M.P. Silva, J. Izquierdo, M.X. Milagre, A.M. Betancor-Abreu, I. Costa, R.M. Souto, Use of amperometric and potentiometric probes in scanning electrochemical microscopy for the spatially-resolved monitoring of severe localized corrosion sites on aluminum alloy 2098-T351, Sensors 21 (2021) 1132, https://doi.org/10.3390/s21041132.
[7] R.M.P. Silva, J. Izquierdo, M.X. Milagre, A.M. Betancor-Abreu, L.A. de Oliveira, R. A. Antunes, R.M. Souto, I. Costa, On the local corrosion behavior of coupled welded zones of the 2098-T351 Al−Cu−Li alloy produced by Friction Stir Welding (FSW): an amperometric and potentiometric microelectrochemical investigation, Electrochim. Acta 373 (2021), 137910, https://doi.org/10.1016/j.electacta.2021.137910.
[8] J.V.S. Araujo, A.F.S. Bugarin, U. Donatus, C.S.C. Machado, F.M. Queiroz, M. Terada, A. Astarita, I. Costa, Thermomechanical treatment and corrosion

resistance correlation in the AA2198 Al−Cu−Li alloy, Corros. Eng., Sci. Technol. 54 (2019) 575–586, https://doi.org/10.1080/1478422X.2019.1637077.
[9] P.L. Threadgill, A.J. Leonard, H.R. Shercliff, P.J. Withers, Friction stir welding of aluminium alloys, Int. Mater. Rev. 54 (2009) 49–93, https://doi.org/10.1179/174328009x411136.
[10] T. Dursun, C. Soutis, Recent developments in advanced aircraft aluminium alloys, Mater. Des. 56 (2014) 862–871, https://doi.org/10.1016/j.matdes.2013.12.002.
[11] U. Donatus, R.M.P. Silva, J.V.S. Araujo, M.X. Milagre, C.P. Abreu, C.S.C. Machado, I. Costa, Macro and microgalvanic interactions in friction stir weldment of AA2198-T851 alloy, J. Mater. Res. Technol. 8 (2019) 6209–6222, https://doi.org/10.1016/j.jmrt.2019.10.015.
[12] L. Niu, Y. Yin, W. Guo, M. Lu, R. Qin, S. Chen, Application of scanning electrochemical microscope in the study of corrosion of metals, J. Mater. Sci. 44 (2009) 4511–4521, https://doi.org/10.1007/s10853-009-3654-x.
[13] M.B. Jensen, D.E. Tallman, Application of SECM to corrosion studies. Electroanalytical Chemistry, in: A.J. Bard, C.G. Zoski (Eds.) 24, CRC Press, Boca Raton, FL, 2012, p. 171.
[14] N.A. Payne, L.I. Stephens, J. Mauzeroll, The application of scanning electrochemical microscopy to corrosion research, Corrosion 73 (2017) 759–780, https://doi.org/10.5006/2354.
[15] A.M. Simões, D. Battocchi, D.E. Tallman, G.P. Bierwagen, SVET and SECM imaging of cathodic protection of aluminium by a Mg-rich coating, Corros. Sci. 49 (2007) 3838–3849, https://doi.org/10.1016/j.corsci.2007.03.045.
[16] R.M. Souto, Y. González-García, D. Battistel, S. Daniele, On the use of mercury-coated tips in scanning electrochemical microscopy to investigate galvanic corrosion processes involving zinc and iron, Corros. Sci. 55 (2012) 401–406, https://doi.org/10.1016/j.corsci.2011.11.003.
[17] S.S. Jamali, S.E. Moulton, D.E. Tallman, M. Forsyth, J. Weber, G.G. Wallace, Applications of scanning electrochemical microscopy (SECM) for local characterization of AZ31 surface during corrosion in a buffered media, Corros. Sci. 86 (2014) 93–100, https://doi.org/10.1016/j.corsci.2014.04.035.
[18] S. Thomas, J. Izquierdo, N. Birbilis, R.M. Souto, Possibilities and limitations of scanning electrochemical microscopy of Mg and Mg alloys, Corrosion 71 (2015) 171–183, https://doi.org/10.5006/1483.
[19] R.M. Souto, J. Izquierdo, J.J. Santana, A. Kiss, L. Nagy, G. Nagy, Progress in scanning electrochemical microscopy by coupling potentiometric and amperometric measurement modes. Current Microscopy Contributions to Advances in Science and Technology,, in: A. Méndez-Vilas (Ed.), in: *Current Microscopy Contributions to Advances in Science and Technology;* A, Volume 2, Formatex Research Center, Badajoz, Spain, 2012, pp. 1407–1415.
[20] E. Tada, S. Satoh, H. Kaneko, The spatial distribution of Zn^{2+} during galvanic corrosion of a Zn/steel couple, Electrochim. Acta 49 (2004) 2279–2285, https://doi.org/10.1016/j.electacta.2004.01.008.
[21] A.C. Bastos, M.G. Taryba, O.V. Karavai, M.L. Zheludkevich, S.V. Lamaka, M.G. S. Ferreira, Micropotentiometric mapping of local distributions of Zn^{2+} relevant to corrosion studies, Electrochem. Commun. 12 (2010) 394–397, https://doi.org/10.1016/j.elecom.2010.01.002.
[22] Á. Varga, L. Nagy, J. Izquierdo, I. Bitter, R. Souto, G. Nagy, Development of solid contact micropipette Zn-ion selective electrode for corrosion studies, Anal. Lett. 44 (2011) 2876–2886, https://doi.org/10.1080/00032719.2011.582545.
[23] J. Izquierdo, L. Nagy, Á. Varga, I. Bitter, G. Nagy, R.M. Souto, Scanning electrochemical microscopy for the investigation of corrosion processes: measurement of Zn^{2+} spatial distribution with ion selective microelectrodes, Electrochim. Acta 59 (2012) 398–403, https://doi.org/10.1016/j.electacta.2011.10.076.
[24] J. Izquierdo, A. Kiss, J.J. Santana, L. Nagy, I. Bitter, H.S. Isaacs, G. Nagy, R. M. Souto, Development of Mg^{2+} ion-selective microelectrodes for potentiometric scanning electrochemical microscopy monitoring of galvanic corrosion processes, J. Electrochem. Soc. 160 (2013) C451–C459, https://doi.org/10.1149/2.001310jes.
[25] S.H. Salleh, N. Birbilis, M. Musameh, K. Venkatesan, S. Thomas, On the development and application of an in-house fabricated Mg^{2+} ion selective microelectrode (ISME) for assessing Mg corrosion, J. Electrochem. Soc. 165 (2018) C771–C776, https://doi.org/10.1149/2.0591811jes.
[26] A. Kiss, D. Filotás, R.M. Souto, G. Nagy, The effect of electric field on potentiometric Scanning Electrochemical Microscopic imaging, Electrochem. Commun. 77 (2017) 138–141, https://doi.org/10.1016/j.elecom.2017.03.011.
[27] D. Filotás, B.M. Fernández-Pérez, A. Kiss, L. Nagy, G. Nagy, R.M. Souto, Double barrel microelectrode assembly to prevent electrical field effects in potentiometric SECM imaging of galvanic corrosion processes, J. Electrochem. Soc. 165 (2018) C270–C277, https://doi.org/10.1149/2.0671805jes.
[28] D. Filotás, B.M. Fernández-Pérez, J. Izquierdo, A. Kiss, L. Nagy, G. Nagy, R. M. Souto, Improved potentiometric SECM imaging of galvanic corrosion reactions, Corros. Sci. 129 (2017) 136–145, https://doi.org/10.1016/j.corsci.2017.10.006.
[29] J.C. Seegmiller, D.A. Buttry, A SECM study of heterogeneous redox activity at AA2024 Surfaces, J. Electrochem. Soc. 150 (2003) B413–B418, https://doi.org/10.1149/1.1593041.
[30] M.B. Jensen, A. Guerard, D.E. Tallman, G.P. Bierwagen, Studies of electron transfer at aluminum alloy surfaces by scanning electrochemical microscopy, J. Electrochem. Soc. 155 (2008) C324–C332, https://doi.org/10.1149/1.2916734.
[31] H. Zhou, X. Li, C. Dong, K. Xiao, T. Li, Corrosion behavior of aluminum alloys in Na_2SO_4 solution using the scanning electrochemical microscopy technique, Int. J. Min, Metall. Mater. 16 (2009) 84–88, https://doi.org/10.1016/S1674-4799(09)60014-5.
[32] J.V.S. Araujo, U. Donatus, F.M. Queiroz, M. Terada, M.X. Milagre, M.C. de Alencar, I. Costa, On the severe localized corrosion susceptibility of the AA2198-T851 alloy, Corros. Sci. 133 (2018) 132–140, https://doi.org/10.1016/j.corsci.2018.01.028.
[33] R.M.P. Silva, M.X. Milagre, L.A. Oliveira, U. Donatus, R.A. Antunes, I. Costa, The local electrochemical behavior of the AA2098-T351 and surface preparation effects investigated by scanning electrochemical microscopy, Surf. Interface Anal. (2019) 982–992, https://doi.org/10.1002/sia.6682.
[34] C.S.C. Machado, R.M.P. da Silva, J.V.S. Araujo, M.X. Milagre, U. Donatus, B.V.G. de Viveiros, R.E. Klumpp, I. Costa, Influence of chloride ions concentration on the development of severe localised corrosion and its effects on the electrochemical response of the 2198-T8 alloy, Corros. Eng., Sci. Technol. 56 (2020) 341–350, https://doi.org/10.1080/1478422X.2020.1862390.
[35] V.K. Gupta, S. Jain, S. Chandra, Chemical sensor for lanthanum(III) determination using aza-crown as ionophore in poly(vinyl chloride) matrix, Anal. Chim. Acta 486 (2003) 199–207, https://doi.org/10.1016/S0003-2670(03)00506-3.
[36] V.K. Gupta, A.K. Jain, S. Agarwal, G. Maheshwari, An iron(III) ion-selective sensor based on a μ-bis(tridentate) ligand, Talanta 71 (2007) 1964–1968, https://doi.org/10.1016/j.talanta.2006.08.038.
[37] V.K. Gupta, A.K. Jain, G. Maheshwari, Manganese (II) selective PVC based membrane sensor using a Schiff base, Talanta 72 (2007) 49–53, https://doi.org/10.1016/j.talanta.2006.09.030.
[38] M.B. Saleh, S.S.M. Hassan, A.A.A. Gaber, N.A.A. Kream, Novel potentiometric membrane sensor for selective determination of aluminum(III) ions, Anal. Chim. Acta 434 (2001) 247–253, https://doi.org/10.1016/S0003-2670(00)01397-0.
[39] L.G. Evsevleeva, L.M. Bykova, V.Y. Badenikov, Aluminum-selective electrode, J. Anal. Chem. 60 (2005) 866–867, https://doi.org/10.1007/s10809-005-0197-4.
[40] A. Yari, L. Darvishi, M. Shamsipur, Al(III)-selective electrode based on newly synthesized xanthone derivative as neutral ionophore, Anal. Chim. Acta 555 (2006) 329–335, https://doi.org/10.1016/j.aca.2005.09.018.
[41] V.K. Gupta, A.K. Jain, G. Maheshwari, Aluminum(III) selective potentiometric sensor based on morin in poly(vinyl chloride) matrix, Talanta 72 (2007) 1469–1473, https://doi.org/10.1016/j.talanta.2007.01.064.
[42] M. Arvand, S.A. Asadollahzadeh, Ion-selective electrode for aluminum determination in pharmaceutical substances, tea leaves and water samples, Talanta 75 (2008) 1046–1054, https://doi.org/10.1016/j.talanta.2008.01.001.
[43] V.K. Gupta, R.N. Goyal, A.K. Jain, R.A. Sharma, Aluminium (III)-selective PVC membrane sensor based on a Schiff base complex of N,N′-bis (salicylidene)-1, 2-cyclohexanediamine, Electrochim. Acta 54 (2009) 3218–3224, https://doi.org/10.1016/j.electacta.2008.11.020.
[44] M. Arvand, M. Kermanian, M.A. Zanjanchi, Direct determination of aluminium in foods and pharmaceutical preparations by potentiometry using an AlMCM-41 modified polymeric membrane sensor, Electrochim. Acta 55 (2010) 6946–6952, https://doi.org/10.1016/j.electacta.2010.06.083.
[45] M. Mokaddem, P. Volovitch, F. Rechou, R. Oltra, K. Ogle, The anodic and cathodic dissolution of Al and Al–Cu–Mg alloy, Electrochim. Acta 55 (2010) 3779–3786, https://doi.org/10.1016/j.electacta.2010.01.079.
[46] M. Serdechnova, P. Volovitch, F. Brisset, K. Ogle, On the cathodic dissolution of Al and Al alloys, Electrochim. Acta 124 (2014) 9–16, https://doi.org/10.1016/j.electacta.2013.09.145.
[47] A. Uhart, J.C. Dupin, J.P. Bonino, D. Gonbeau, J. Esteban, J.B. Ledeuil, F. Ansart, An Auger and XPS survey of cerium active corrosion protection for AA2024-T3 aluminum alloy, Appl. Surf. Sci. 390 (2016) 751–759, https://doi.org/10.1016/j.apsusc.2016.08.170.